The lowest detected stellar Fe abundance: the halo star SMSS J160540.18−144323.1

T. Nordlander [1,2]★ M. S. Bessell [1,2] G. S. Da Costa [1] A. D. Mackey [1,2]
M. Asplund [1,2] A. R. Casey [3,4] A. Chiti,[5] R. Ezzeddine,[5,6] A. Frebel [5,6] K. Lind,[7,8]
A. F. Marino [1,9] S. J. Murphy [1,10] J. E. Norris,[1] B. P. Schmidt [1] and D. Yong [1,2]

[1]*Research School of Astronomy and Astrophysics, Australian National University, Canberra, ACT 2611, Australia*
[2]*ARC Centre of Excellence for All Sky Astrophysics in 3 Dimensions (ASTRO 3D), Australia*
[3]*School of Physics & Astronomy, Monash University, Clayton, VIC 3800, Australia*
[4]*Faculty of Information Technology, Monash University, Clayton, VIC 3800, Australia*
[5]*Department of Physics & Kavli Institute for Astrophysics and Space Research, Massachusetts Institute of Technology, Cambridge, MA 02139, USA*
[6]*Joint Institute for Nuclear Astrophysics – Center for Evolution of the Elements, East Lansing, MI 48824, USA*
[7]*Max-Planck-Institut für Astronomie, Königstuhl 17, D-69117 Heidelberg, Germany*
[8]*Observational Astrophysics, Department of Physics and Astronomy, Uppsala University, Box 516, SE-75120 Uppsala, Sweden*
[9]*Dipartimento di Fisica e Astronomia Galileo Galilei, Univ. di Padova, Vicolo dellOsservatorio 3, Padova I-35122, Italy*
[10]*School of Science, University of New South Wales, Canberra, ACT 2600, Australia*

ABSTRACT

We report the discovery of SMSS J160540.18−144323.1, a new ultra metal-poor halo star discovered with the SkyMapper telescope. We measure $[Fe/H] = -6.2 \pm 0.2$ (1D LTE), the lowest ever detected abundance of iron in a star. The star is strongly carbon-enhanced, $[C/Fe] = 3.9 \pm 0.2$, while other abundances are compatible with an α-enhanced solar-like pattern with $[Ca/Fe] = 0.4 \pm 0.2$, $\big[Mg/Fe\big] = 0.6 \pm 0.2$, $[Ti/Fe] = 0.8 \pm 0.2$, and no significant s- or r-process enrichment, $[Sr/Fe] < 0.2$ and $[Ba/Fe] < 1.0$ (3σ limits). Population III stars exploding as fallback supernovae may explain both the strong carbon enhancement and the apparent lack of enhancement of odd-Z and neutron-capture element abundances. Grids of supernova models computed for metal-free progenitor stars yield good matches for stars of about $10\,M_\odot$ imparting a low kinetic energy on the supernova ejecta, while models for stars more massive than roughly $20\,M_\odot$ are incompatible with the observed abundance pattern.

Key words: stars: abundances – stars: individual: SMSS J160540.18−144323.1 – stars: Population III.

1 INTRODUCTION

The early evolution of the Universe depends on the properties of the first generation of metal-free stars, the so-called Population III, and in particular on their mass as well as properties of their supernova explosions. High-mass Population III stars were short-lived, and can only be studied indirectly through their supernova ejecta that enriched the gas clouds from which the oldest metal-poor (but not metal-free) stars formed which are still observable today.

Targeted efforts by several groups (e.g. Beers, Preston & Shectman 1985; Christlieb 2003; Keller et al. 2007; Caffau et al. 2013; Aguado et al. 2017; Starkenburg et al. 2017) have led to the

discovery of roughly 30 stars with $[Fe/H] < -4$[1] (Abohalima & Frebel 2018), where the most iron-poor stars in fact only have upper limits. In particular, SMSS 0313−6708 at $[Fe/H] < -7.3$ (Keller et al. 2014; Nordlander et al. 2017) and J0023+0307 at $[Fe/H] < -5.8$ (Aguado et al. 2018; Frebel et al. 2019) both have abundance patterns that indicate true iron abundances (predicted from Population III star supernova models) significantly lower than their detection limits. The most iron-poor stars where iron has actually been detected are HE 1327−2326 at $[Fe/H] = -5.7$ (Frebel et al. 2005; Aoki et al. 2006), HE 0107−5240 at $[Fe/H] = -5.4$ (Christlieb et al. 2002, 2004), and SD 1313−0019 at $[Fe/H] = -5.0$ (Allende Prieto et al. 2015; Frebel et al. 2015). All five stars exhibit strong carbon enhancement and typically strong odd–even effects

---

★ E-mail: Thomas.Nordlander@anu.edu.au

[1]Throughout this discussion we use the 1D LTE abundance values.

that are similar to predictions for Population III star supernovae with masses between 10 and $60\,M_\odot$, and explosion energies less than 10^{51} erg assuming a mixing and fallback explosion mechanism (Heger & Woosley 2010; Ishigaki et al. 2014). In particular for the two stars that have only upper limits on their iron abundance, the comparison is not well constrained and matches instead for a wide range of progenitor mass and explosion energy (Nordlander et al. 2017; Frebel et al. 2019). This happens because the iron abundance is sensitive to processes that occur near the iron core of the progenitor star, e.g. the amount of mixing driven by Rayleigh–Taylor instabilities, the location where the explosion originates, and the explosion energy that determines whether ejecta subsequently fall back on to the newly formed black hole (see discussion in Ishigaki et al. 2014).

We have recently discovered SMSS J160540.18−144323.1 (hereafter SMSS 1605−1443), a red giant branch star with the lowest ever detected abundance of iron, [Fe/H] = −6.2 ± 0.2. The fact that iron has been detected alongside carbon, magnesium, calcium, and titanium, offers for the first time strong constraints on chemical enrichment at this metallicity. We give here an assessment of its stellar parameters and chemical composition based on the spectra acquired during discovery and verification.

2 OBSERVATIONS

SMSS 1605−1443 (g = 16.0) was discovered as part of the SkyMapper search for extremely metal-poor stars (Keller et al. 2007; Da Costa et al. 2019) using the metallicity-sensitive narrow-band v-filter in SkyMapper DR1.1 (Wolf et al. 2018). The star was confirmed to have [Fe/H] < −5 from medium-resolution (R = 3000 and R = 7000) spectrophotometry acquired in 2018 March and August with the WIFES spectrograph (Dopita et al. 2010) on the ANU 2.3-m telescope. The photometric selection and confirmation methodology is described further elsewhere (Jacobson et al. 2015; Da Costa et al. 2019; Marino et al. 2019). Follow-up high-resolution spectra were taken on the night of 2018 September 1 in 1 arcsec seeing with the MIKE spectrograph (Bernstein et al. 2003) at the 6.5-m Magellan Clay telescope. We used a 1 arcsec slit and 2 × 2 binning, producing a spectral resolving power $R = \lambda/\Delta\lambda = 28\,000$ on the blue detector and 22 000 on the red detector. We reduced data using the CARPY pipeline (Kelson 2003). Coadding the 4 × 1800 s exposures resulted in a signal to noise per pixel, S/N ≈ 10 at 3700 Å, 30 at 4000 Å, and 90 at 6700 Å.

3 METHODS

We fit the observed high- and medium-resolution spectra using χ^2 statistics. Upper limits to abundances were determined using a likelihood estimate assuming Gaussian errors, considering multiple lines simultaneously where applicable. While fitting, the synthetic spectra are convolved with a Gaussian profile representing the instrumental profile. We determine the continuum placement by taking the median ratio between the observed and synthetic spectrum in continuum windows that are predicted to be free of line absorption. In the spectrophotometric analysis, the slope of the continuum is matched by applying the R_V = 3.1 reddening law from Fitzpatrick (1999) to the synthetic spectra.

For the spectrophotometric analysis, we compute a comprehensive grid of 1D LTE spectra using the TURBOSPECTRUM code (v15.1; Alvarez & Plez 1998; Plez 2012) and MARCS model atmospheres (Gustafsson et al. 2008). We use v_{mic} = 2 km s^{-1} and perform the radiative transport under spherical symmetry taking into account

continuum scattering. The spectra are computed with a sampling step of 1 km s^{-1}, corresponding to a resolving power $R \approx 300\,000$. We adopt the solar chemical composition and isotopic ratios from Asplund et al. (2009), but assume $[\alpha/\text{Fe}] = 0.4$ and compute spectra with varying carbon abundance. For our high-resolution spectroscopic abundance analyses, we compute additional grids where we vary the overall metallicity as well as the abundance of carbon and one additional element at a time. We also use the 3D NLTE hydrogen Balmer line profiles from Amarsi et al. (2018).

For all 1D LTE grids, we use a selection of atomic lines from VALD3 (Ryabchikova et al. 2015) together with roughly 15 million molecular lines representing 18 different molecules, the most important of which for this work being those for CH (Masseron et al. 2014) and CN (Brooke et al. 2014; Sneden et al. 2014).

4 RESULTS

4.1 Stellar parameters

We find consistent stellar parameters from medium-resolution spectrophotometry, optical and infrared photometry, high-resolution Balmer line analyses, and stellar evolution constraints, and illustrate our synthetic spectrum fits in Fig. 1.

Our spectrophotometric analysis of the initial medium-resolution spectrum indicates T_{eff} = 4925 K, $\log g$ = 2.0, and [Fe/H] < −4.75 (see Da Costa et al. 2019). We assumed a reddening value $E(B - V)$ = 0.20 based on the dust map from Schlegel et al. (1998, rescaled according to Wolf et al. 2018). This is similar to the distance-dependent dust map of Green et al. (2018) that indicates $E(B - V)$ = 0.23 ± 0.02. The interstellar lines of Na ID 5890 Å and K I 7699 Å show a complex structure of multiple components, indicating $E(B - V)$ between 0.12 and 0.21 using the calibrations of Munari & Zwitter (1997) and Poznanski, Prochaska & Bloom (2012). Adopting this range in reddening, we find good spectrophotometric fits for T_{eff} = 4900 ± 100 K, $\log g$ = 2.0 ± 0.2. The infrared flux method calibrations on SkyMapper and 2MASS photometry from Casagrande et al. (2019) indicate T_{eff} = 4865 ± 34 ± 117 K from $g - K_s$ and 4784 ± 59 ± 83 K from $z - K_s$, where the error bars represent the uncertainties due to the measurement and reddening, respectively.

We fit 3D NLTE Balmer line profiles (Amarsi et al. 2018) to the high-resolution spectrum, taking care to avoid telluric lines for Hα as well as lines of CH that contaminate Hγ and Hβ. We find good simultaneous fits for all three Balmer lines with T_{eff} = 4850 ± 100 K and $\log g$ = $2.0^{+0.5}_{-0.3}$. These reddening-free estimates are in excellent agreement with the aforementioned spectrophotometric and photometric values, and we therefore adopt as our final parameters: T_{eff} = 4850 ± 100 K, $\log g$ = 2.0 ± 0.2 dex. With these stellar parameters, the spectrophotometry indicates $E(B - V)$ = 0.12, in agreement with the strengths of interstellar lines.

Placco et al. (2014) present stellar evolution models that take into account varying enhancement of carbon and nitrogen. The fact that nitrogen is not detected in SMSS 1605−1443 implies that the episode of extra mixing usually associated with thermohaline mixing (Eggleton, Dearborn & Lattanzio 2006; Charbonnel & Zahn 2007) has not yet occurred, and further that the surface abundance of carbon is not depleted (<0.01 dex). This extra mixing episode is associated with significant theoretical uncertainty, both in the magnitude of effects and the evolutionary stage where they occur (Angelou et al. 2011; Henkel, Karakas & Lattanzio 2017; Shetrone et al. 2019). Taking into account the systematic corrections discussed by Placco et al. (2014), our non-detection of
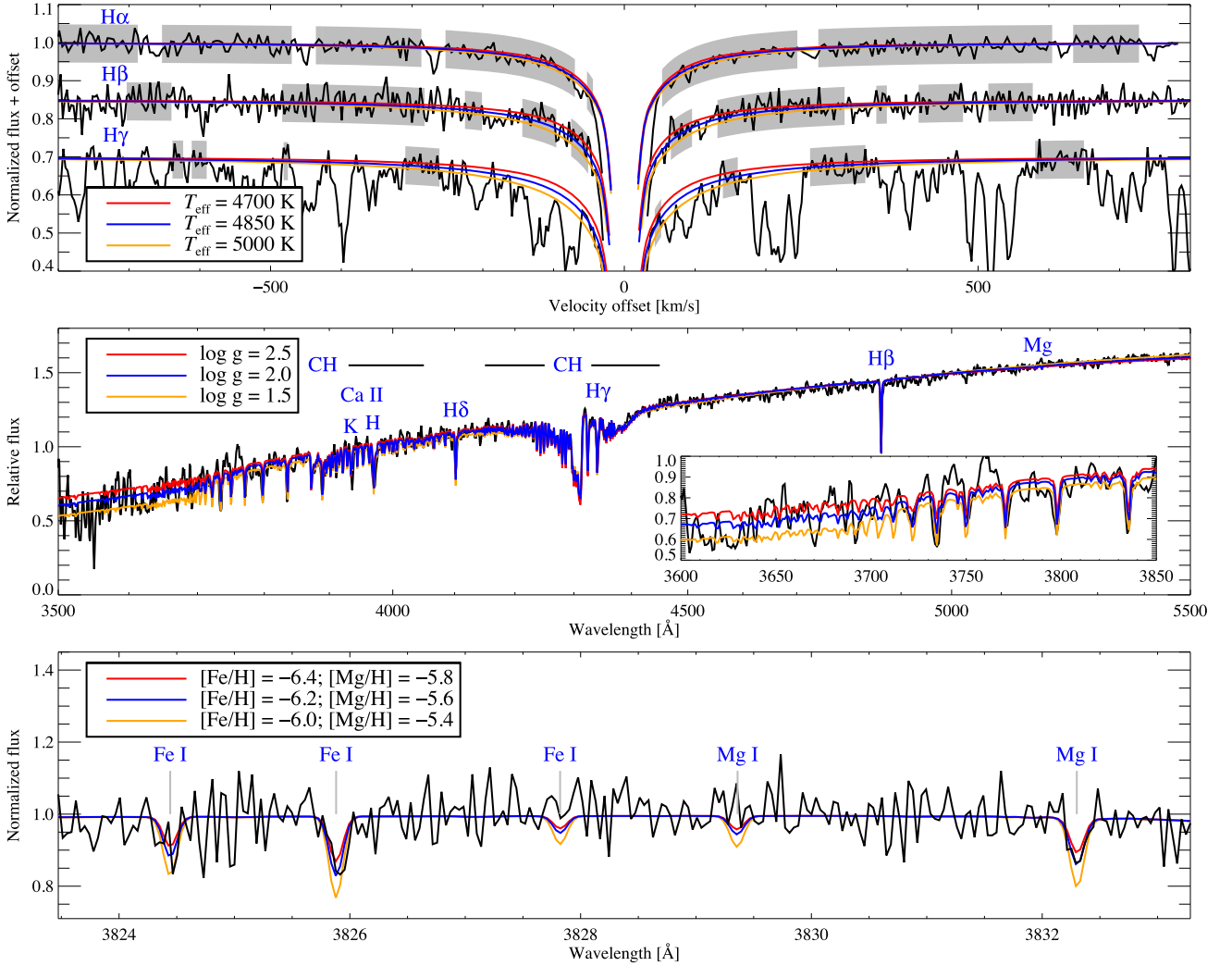
Figure 1. *Upper panel*: Fit of the effective temperature to the first three Balmer lines (labelled) in the MIKE high-resolution spectrum, compared to models at the preferred $T_{\text{eff}} = 4850$ K. The lines are shown on a velocity scale centred on each line, and have been offset vertically. The grey shaded blocks represent the wavelength ranges used in the χ^2 minimization. *Middle panel*: Fit of the surface gravity to the WiFeS medium-resolution spectrophotometry, with a zoomed inset showing the Balmer jump region, at the preferred $\log g = 2.0$. *Lower panel*: Example fits to lines of Fe and Mg in the MIKE high-resolution spectrum. In all panels additional models illustrate the sensitivity, and the legend lists the models as shown from top to bottom.

nitrogen constrains $\log g > 1.9$, in agreement with our spectroscopic measurements.

The *Gaia* DR2 parallax measurement, $\pi = 0.0004 \pm 0.0544$ mas (Gaia Collaboration et al. 2016, 2018), yields a lower limit to the distance to SMSS 1605−1443 implying $\log g < 2.5$ (3σ). Conversely, our spectroscopic estimate of $\log g = 2.0 \pm 0.2$ implies a predicted parallax of $\pi = 0.09 \pm 0.02$ mas, i.e. a distance of 11 ± 3 kpc, placing it on the other side of the Galaxy. We note that its kinematics (with $v_{\text{rad}} = -224$ km s^{-1}) indicate it being a normal inner halo star.

4.2 Abundance analysis

We report results of our abundance analysis in Table 1, where statistical uncertainties on the absolute abundance are based on our χ^2 analyses and upper limits are given at the 3σ level. The systematic errors on the absolute abundances are estimated by changing the stellar parameters (T_{eff}, $\log g$, [Fe/H] and [C/H]), one at a time according to their estimated uncertainty, and adding the

effects in quadrature. We do not attempt to quantify the influence of hydrodynamic and non-LTE effects (e.g. Amarsi et al. 2016; Nordlander et al. 2017), but defer this to future work that incorporates a full 3D non-LTE analysis and higher quality observations (Nordlander et al., in preparation).

We estimate the iron abundance from a set of 16 lines of Fe I, 10 detected and 6 upper limits, with lower excitation potential E_{low} between 0 and 1.5 eV. Using a maximum-likelihood estimate that also takes into account the six lines that have only upper limits, we find a mean abundance [Fe/H] $= -6.21 \pm 0.17$, with a flat trend -0.01 ± 0.14 dex eV^{-1} as a function of E_{low}. Fe II cannot be detected using the current spectrum. The three strongest lines yield an upper limit [Fe/H] < -4.7 (3σ).

We estimate a carbon abundance [C/H] $= -2.32 \pm 0.05$ using CH lines from the $A^2\Delta - X^2\Pi$ system at 4100–4400 Å and the $B^2\Sigma^- - X^2\Pi$ system at 3900 Å. We do not detect absorption due to ^{13}CH, and refrain from placing a limit on the isotopic ratio. For magnesium, we measure [Mg/H] $= -5.65 \pm 0.13$ from the UV triplet at 3829–3838 Å. We find an equivalent width of just 17 mÅ for the only

Table 1. High-resolution spectroscopic 1D LTE abundance analysis. Upper limits are given at the 3σ level. Error estimates on the absolute abundances are reported for both the statistical measurement uncertainty (σ_{stat}) and the systematic uncertainty due to uncertainties in stellar parameters (σ_{sys}). The last column gives the reference solar chemical composition.

Species	$A(X)$	[X/H]	[X/Fe]	σ_{stat}	σ_{sys}	$A(X)_\odot$
Li I	<0.48	<−0.57	<5.64	0.18	0.09	1.05
C (CH)	6.07	−2.32	3.89	0.05	0.27	8.39
N (CN)	<4.80	<−2.98	<3.23	0.19	0.18	7.78
O I	<7.21	<−1.48	<4.73	0.19	0.15	8.69
Na I	<0.90	<−5.27	<0.94	0.18	0.10	6.17
Mg I	1.88	−5.65	0.57	0.13	0.09	7.53
Al I	<0.67	<−5.76	<0.45	0.19	0.11	6.43
Si I	<2.09	<−5.42	<0.80	0.20	0.11	7.51
K I	<1.98	<−3.10	<3.11	0.19	0.09	5.08
Ca I	0.46	−5.85	0.37	0.11	0.13	6.31
Ca II	1.24	−5.07	1.15	0.05	0.15	6.31
Sc II	<−1.76	<−4.93	<1.29	0.12	0.10	3.17
Ti II	−0.50	−5.40	0.82	0.10	0.10	4.90
V II	<0.69	<−3.31	<2.90	0.23	0.09	4.00
Cr I	<0.22	<−5.42	<0.79	0.20	0.13	5.64
Mn I	<0.03	<−5.36	<0.85	0.19	0.15	5.39
Fe I	1.24	−6.21	...	0.17	0.14	7.45
Fe II	<2.72	<−4.73	...	0.18	0.06	7.45
Co I	<0.56	<−4.36	<1.85	0.19	0.14	4.92
Ni I	<0.87	<−5.36	<0.85	0.25	0.14	6.23
Cu I	<1.51	<−2.70	<3.51	0.19	0.12	4.21
Zn I	<1.55	<−3.05	<3.16	0.19	0.06	4.60
Sr II	<−3.12	<−6.04	<0.17	0.19	0.10	2.92
Ba II	<−3.07	<−5.24	<0.97	0.19	0.11	2.17
Eu II	<−2.41	<−2.93	<3.28	0.19	0.11	0.52

Figure 2. Comparison of the measured abundances (blue squares) and 3σ upper limits (blue arrows) to yields from Population III supernova models with varying progenitor star mass, explosion energy (in units of 10^{51} erg = 1 B), and mixing parameter. No satisfactory fit to the observed abundance pattern exists for models more massive than about 20 $M_\odot$.

detectable Mg Ib line at 5185 Å. For calcium, the Ca II H and K lines indicate [Ca/H] = -5.07 ± 0.05. We also measure [Ca/H] = -5.85 ± 0.11 from Ca I 4226 Å, resulting in a very large 0.8 dex abundance difference between the two ionization stages. This is likely mainly due to the non-LTE overionization of Ca I as well as a smaller non-LTE effect of opposite sign acting on Ca II (see e.g. Sitnova et al. 2019). Comparing the measured abundances of Ca I and Fe I, this implies a normal level of α-enhancement as seen in most halo stars, [Ca/Fe] = 0.37 ± 0.20. For titanium we detect the two lines of Ti II at 3759–3761 Å and obtain [Ti/H] = -5.40 ± 0.10.

We determine upper limits for additional elements using a likelihood estimate that assumes Gaussian errors. We use synthetic spectra for these estimates, and consider multiple lines simultaneously when applicable.

5 DISCUSSION

Our analysis of SMSS 1605−1443 reveals remarkably low abundances of heavier elements, including the lowest ever measured abundance of iron at [Fe/H] = -6.2 ± 0.2. While the abundance pattern from Na to Zn is broadly compatible with a standard α-enhanced chemical composition typical of halo stars, the large carbon enhancement is a strong indicator for enrichment from a Population III mixing-and-fallback supernova (see e.g. Umeda & Nomoto 2002; Nomoto, Kobayashi & Tominaga 2013). Using the predicted supernova yields computed for metal-free Population III stars by Heger & Woosley (2010), we find a reasonable match only for low-mass progenitors ($M \approx 10 \, M_\odot$) with low explosion energy ($<10^{51}$ erg), as shown in Fig. 2. Models more massive than
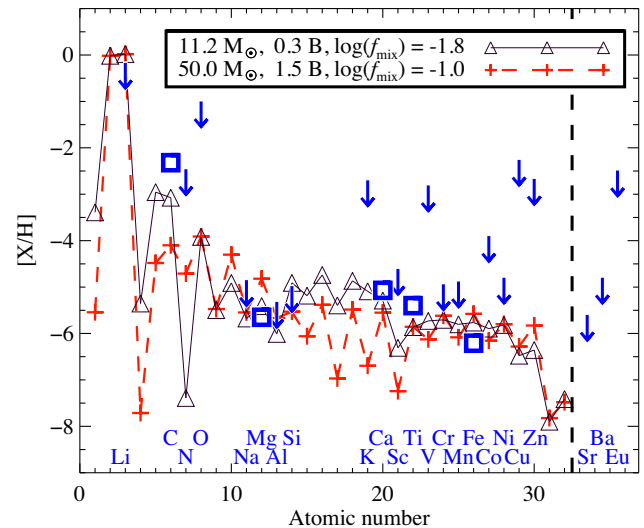
about 20 $M_\odot$ cannot simultaneously reproduce the strong carbon enhancement and the otherwise flat abundance trend.

Alternative explanations for the carbon enhancement are unsatisfactory. Pollution from an intermediate-mass companion star is predicted to also bring similar enhancement of nitrogen and neutron-capture elements (Campbell & Lattanzio 2008; Campbell, Lugaro & Karakas 2010; Cruz, Serenelli & Weiss 2013). Similarly, the i-process appears to overproduce Na and possibly neutron-capture elements (Clarkson, Herwig & Pignatari 2018). Late accretion from the ISM could also enhance carbon, but models of this process also predict significant enhancement of nitrogen (Johnson 2015), and can likewise be ruled out.

It has been shown in previous work (Collet, Asplund & Trampedach 2006; Frebel et al. 2008; Caffau et al. 2012; Bessell et al. 2015; Nordlander et al. 2017) that significant systematic uncertainties are associated with the chemical abundance analyses of the most iron-poor stars. We note that these corrections depend sensitively on not only the effective temperature and surface gravity of the star, but also the abundance of the element under study, and we caution against blindly applying representative corrections. Although these effects may be as large as 1 dex, they are unlikely to significantly alter the main conclusions of this work: It is clear that SMSS 1605−1443 is the most iron-deficient star for which iron has been detected, that it is strongly carbon enhanced, and that it does not exhibit strong enhancement nor a strong abundance trend among elements heavier than carbon. A higher quality spectrum would enable more stringent limits and likely detections of additional elements, which together with advanced spectrum synthesis techniques will allow us to better understand the properties of the Population III progenitor star.

REFERENCES

Abohalima A., Frebel A., 2018, ApJS, 238, 36

Aguado D. S., Allende Prieto C., González Hernández J. I., Rebolo R., 2018, ApJ, 854, L34

Aguado D. S., Allende Prieto C., González Hernández J. I., Rebolo R., Caffau E., 2017, A&A, 604, A9

Allende Prieto C. et al., 2015, A&A, 579, A98

Alvarez R., Plez B., 1998, A&A, 330, 1109

Amarsi A. M., Lind K., Asplund M., Barklem P. S., Collet R., 2016, MNRAS, 463, 1518

Amarsi A. M., Nordlander T., Barklem P. S., Asplund M., Collet R., Lind K., 2018, A&A, 615, A139

Angelou G. C., Church R. P., Stancliffe R. J., Lattanzio J. C., Smith G. H., 2011, ApJ, 728, 79

Aoki W. et al., 2006, ApJ, 639, 897

Asplund M., Grevesse N., Sauval A. J., Scott P., 2009, ARA&A, 47, 481

Beers T. C., Preston G. W., Shectman S. A., 1985, AJ, 90, 2089

Bernstein R., Shectman S. A., Gunnels S. M., Mochnacki S., Athey A. E., 2003, in Iye M., Moorwood A. F. M., eds, Proc. SPIE Conf. Ser. Vol. 4841, Instrument Design and Performance for Optical/Infrared Ground-Based Telescopes. SPIE, Bellingham, p. 1694

Bessell M. S. et al., 2015, ApJ, 806, L16

Brooke J. S. A., Ram R. S., Western C. M., Li G., Schwenke D. W., Bernath P. F., 2014, ApJS, 210, 23

Caffau E. et al., 2012, A&A, 542, A51

Caffau E. et al., 2013, A&A, 560, A71

Campbell S. W., Lattanzio J. C., 2008, A&A, 490, 769

Campbell S. W., Lugaro M., Karakas A. I., 2010, A&A, 522, L6

Casagrande L., Wolf C., Mackey A. D., Nordlander T., Yong D., Bessell M., 2019, MNRAS, 482, 2770

Charbonnel C., Zahn J.-P., 2007, A&A, 467, L15

Christlieb N., 2003, Scheilicke R. E., in The Cosmic Circuit of Matter. Reviews in Modern Astronomy, Vol. 16. Wiley, New York. p. 191

Christlieb N., Gustafsson B., Korn A. J., Barklem P. S., Beers T. C., Bessell M. S., Karlsson T., Mizuno-Wiedner M., 2004, ApJ, 603, 708

Christlieb N. et al., 2002, Nature, 419, 904

Clarkson O., Herwig F., Pignatari M., 2018, MNRAS, 474, L37

Collet R., Asplund M., Trampedach R., 2006, ApJ, 644, L121

Cruz M. A., Serenelli A., Weiss A., 2013, A&A, 559, A4

Da Costa G. S. et al., 2019, MNRAS, submitted

Dopita M. et al., 2010, Ap&SS, 327, 245

Eggleton P. P., Dearborn D. S. P., Lattanzio J. C., 2006, Science, 314, 1580

Fitzpatrick E. L., 1999, PASP, 111, 63

Frebel A., Chiti A., Ji A. P., Jacobson H. R., Placco V. M., 2015, ApJ, 810, L27

Frebel A., Collet R., Eriksson K., Christlieb N., Aoki W., 2008, ApJ, 684, 588

Frebel A., Ji A. P., Ezzeddine R., Hansen T. T., Chiti A., Thompson I. B., Merle T., 2019, ApJ, 871, 146

Frebel A. et al., 2005, Nature, 434, 871

Gaia Collaboration et al., 2016, A&A, 595, A1

Gaia Collaboration et al., 2018, A&A, 616, A1

Green G. M. et al., 2018, MNRAS, 478, 651

Gustafsson B., Edvardsson B., Eriksson K., Jørgensen U. G., Nordlund A., Plez B., 2008, A&A, 486, 951

Heger A., Woosley S. E., 2010, ApJ, 724, 341

Henkel K., Karakas A. I., Lattanzio J. C., 2017, MNRAS, 469, 4600

Ishigaki M. N., Tominaga N., Kobayashi C., Nomoto K., 2014, ApJ, 792, L32

Jacobson H. R. et al., 2015, ApJ, 807, 171

Johnson J. L., 2015, MNRAS, 453, 2771

Keller S. C. et al., 2007, Publ. Astron. Soc. Aust., 24, 1

Keller S. C. et al., 2014, Nature, 506, 463

Kelson D. D., 2003, PASP, 115, 688

Marino A. F. et al., 2019, MNRAS, 485, 5153

Masseron T. et al., 2014, A&A, 571, A47

Munari U., Zwitter T., 1997, A&A, 318, 269

Nomoto K., Kobayashi C., Tominaga N., 2013, ARA&A, 51, 457

Nordlander T., Amarsi A. M., Lind K., Asplund M., Barklem P. S., Casey A. R., Collet R., Leenaarts J., 2017, A&A, 597, A6

Placco V. M., Frebel A., Beers T. C., Stancliffe R. J., 2014, ApJ, 797, 21

Plez B., 2012, Astrophysics Source Code Library, record ascl:1205.004

Poznanski D., Prochaska J. X., Bloom J. S., 2012, MNRAS, 426, 1465

Ryabchikova T., Piskunov N., Kurucz R. L., Stempels H. C., Heiter U., Pakhomov Y., Barklem P. S., 2015, Phys. Scr., 90, 054005

Schlegel D. J., Finkbeiner D. P., Davis M., 1998, ApJ, 500, 525

Shetrone M. et al., 2019, ApJ, 872, 137

Sitnova T. M., Mashonkina L. I., Ezzeddine R., Frebel A., 2019, MNRAS, 485, 3527

Sneden C., Lucatello S., Ram R. S., Brooke J. S. A., Bernath P., 2014, ApJS, 214, 26

Starkenburg E. et al., 2017, MNRAS, 471, 2587

Umeda H., Nomoto K., 2002, ApJ, 565, 385

Wolf C. et al., 2018, Publ. Astron. Soc. Aust., 35, e010

This paper has been typeset from a TeX/LaTeX file prepared by the author.